remote sensing

MDPI

Article

The Indian Ocean Dipole Modulates the Phytoplankton Size Structure in the Southern Tropical Indian Ocean

Xiaomei Liao [1], Yan Li [1,*], Weikang Zhan [2,3], Qianru Niu [1] and Lin Mu [1]

[1] College of Life Sciences and Oceanography, Shenzhen University, Shenzhen 518060, China; liaoxm@szu.edu.cn (X.L.); qniu@szu.edu.cn (Q.N.); mulin@szu.edu.cn (L.M.)
[2] State Key Laboratory of Tropical Oceanography, South China Sea Institute of Oceanology, Chinese Academy of Sciences, Guangzhou 510301, China; wkzhan@scsio.ac.cn
[3] Guangdong Key Lab of Ocean Remote Sensing, South China Sea Institute of Oceanology, Chinese Academy of Sciences, Guangzhou 510301, China
* Correspondence: liyan_ocean@szu.edu.cn

Abstract: The phytoplankton size structure exerts a significant influence on ecological processes and biogeochemical cycles. In this study, the interannual variations in remotely sensed phytoplankton size structure in the southern Tropical Indian Ocean (TIO) and the underlying physical mechanisms were investigated. Significant interannual fluctuations in phytoplankton size structure occur in the southeastern TIO and central southern TIO and are very sensitive to Indian Ocean Dipole (IOD) events. During positive IOD events, the southeast wind anomalies reinforce coastal upwelling off of Java and Sumatra, leading to a shift toward a larger phytoplankton structure in the southeastern TIO. The anomalous anticyclonic circulation deepened the thermocline and triggered the oceanic downwelling Rossby waves, resulting in a smaller phytoplankton structure in the southwestern TIO. During the decay phase of the strong positive IOD events, the sustained warming in the southwestern TIO induced basin-wide warming, thereby maintaining such an anomalous phytoplankton size structure into the following spring. The response of phytoplankton size structure and ocean dynamics displayed inverse patterns during the negative IOD events, with an anomalous larger phytoplankton structure in the central southern TIO. These findings enhance our understanding of phytoplankton responses to climate events, with serious implications for ecosystem changes in a warming climate.

Keywords: phytoplankton size structure; interannual variations; physical processes; Indian Ocean Dipole; Tropical Indian Ocean

Citation: Liao, X.; Li, Y.; Zhan, W.; Niu, Q.; Mu, L. The Indian Ocean Dipole Modulates the Phytoplankton Size Structure in the Southern Tropical Indian Ocean. *Remote Sens.* **2024**, *16*, 1970. https://doi.org/10.3390/rs16111970

Academic Editor: Raphael M. Kudela

Received: 15 April 2024
Revised: 25 May 2024
Accepted: 29 May 2024
Published: 30 May 2024

1. Introduction

Phytoplankton play a fundamental role as primary producers in marine ecosystems. Phytoplankton cell size, a crucial indicator of phytoplankton community dynamics in the ocean, is typically categorized into three size fractions: picophytoplankton (0.2–2 μm), nanophytoplankton (2–20 μm), and microphytoplankton (20–200 μm) [1]. Phytoplankton size affects their physiological characteristics and their roles in ecosystems and biogeochemical processes, regulating the energy transfer efficiency of marine ecosystems [2]. For instance, larger phytoplankton cells support a highly efficient biological pump due to their faster sinking rates. Phytoplankton size structure is thus important to many fundamental biogeochemical processes, including nutrient uptake and cycling, energy transfer through the marine food web, and deep-ocean carbon export [3].

The size structure of the phytoplankton community exerts a size-dependent influence on the inherent optical properties of the water column, including absorption and backscattering coefficients [4,5]. In the global oceans, the distribution of phytoplankton cell size is closely related to nutrient supply. Large phytoplankton are more prevalent in turbulent and nutrient-rich waters (e.g., upwelling zones), while small phytoplankton are commonly found in stratified and oligotrophic waters [6]. These variations in phytoplankton size structure

have been demonstrated to be regulated by the redistribution of nutrients induced by oceanic dynamics. Physical processes, such as upwelling, ocean circulation and surface stratification, affect nutrient supply and consequently lead to changes in phytoplankton size structure [2,7,8].

The satellite remote sensing of ocean color is a key method currently available for synoptically measuring the wide-area properties of ocean ecosystems, such as phytoplankton size [5,6]. Various methods have been developed for the retrieval of global phytoplankton size structure data using satellite ocean-color observations. Present methodologies for determining phytoplankton size from satellite observations in Case 1 waters can be categorized into two primary categories: abundance-based approaches (uni-variate) [6,9,10] and spectral-based approaches (multi-variate) [3,4,11–13]. Abundance-based algorithms depend on observed relationships between phytoplankton abundance and their size structure, while spectral-based approaches rely on optical properties such as the phytoplankton absorption coefficient and the particle backscattering coefficient [3]. Kostadinov et al. [4] estimated global phytoplankton size structure by analyzing the particle size distribution (PSD) through the backscattering slope. However, the particle size classes include all particles, not just phytoplankton. Roy et al. [13] reconstructed the PSD model using a chlorophyll-a (*Chl*)-specific absorption coefficient at a red wavelength (676 nm). Waga et al. [14] developed a *Chl* size distribution (CSD) model based on empirical relationships between the size distribution of *Chl* and the spectral shape of the absorption coefficient of the phytoplankton.

Due to advancements in algorithm development and the increasing availability of ocean observations, many studies have analyzed the seasonal and interannual variations in large-scale phytoplankton size structure, as well as their relationship with oceanic dynamic processes and their responses to climatic events [2,15,16]. Phytoplankton size structure or phytoplankton community composition has been observed to vary with temperature, with an increasing prevalence of small cells within oceanic communities as temperatures rise [17]. Utilizing satellite ocean-color data and an ocean biogeochemical model, Arteaga and Rousseaux [15] revealed that warm sea surface temperature (SST) anomalies in the northeastern Pacific Ocean lead to changes in phytoplankton community composition. The 2016 El Niño event triggered an almost total collapse of diatoms, resulting in a sharp decrease in surface chlorophyll (*Chl*) concentrations.

The southern Tropical Indian Ocean (TIO) is recognized as the region with the shallowest thermocline in the TIO, primarily maintained by the upwelling induced by the negative wind stress curl between the weak equatorial westerlies and the southeasterly trades over the TIO [18,19]. The variability of phytoplankton in the southern TIO displays prominent seasonal patterns, with the most notable variations observed within the 5°–12°S latitude band. This region is oligotrophic during the monsoon transition seasons, which occur from March to May (MAM) and September to November (SON). Chlorophyll blooms occur during the boreal summer monsoon season (June to August, JJA), while episodic blooms are observed during the winter monsoon season (December to February, DJF) [20]. Besides seasonal variations, the shallow thermocline in the southern TIO makes it particularly sensitive to climatic events [18,21]. Interannual variations in phytoplankton in this region are markedly coupled with the Indian Ocean Dipole (IOD) or El Niño-Southern Oscillation (ENSO) [20,22–24]. During positive (negative) IOD events, upwelling-favorable winds in the southeastern TIO were enhanced (weakened), leading to higher (lower) *Chl* concentrations, whereas *Chl* concentrations decreased (increased) in the western TIO [25]. Other physical processes, including boundary current, the turbulent mixing associated with the surface current and subsurface equatorial undercurrent [23,26], and advection by Indonesian throughflow [19,27], contribute to the interannual variability of *Chl* in the southeastern TIO. Pronounced variations in *Chl* are observed in the southern TIO during extreme IOD events or in years when both IOD and ENSO occur simultaneously, driven by anomalous atmospheric circulation and associated oceanic Rossby waves [28,29].

Even though the dynamics and variability of *Chl* impacted by the IOD or ENSO in the TIO have received considerable attention, less is known about the interannual variability of phytoplankton size structure. Brewin et al. [2] employed a three-component

remote sensing retrieval model based on *Chl* concentrations to explore the influence of the IOD on phytoplankton size structure. Their study revealed a significant alteration in the phytoplankton size structure observed in the eastern equatorial Indian Ocean in December 1997, and the variation in phytoplankton size structure was found to be closely associated with changes in SST and sea surface height (SSH) anomalies. However, the spatiotemporal characteristics and associated physical mechanisms of the response of phytoplankton size structure to the IOD remain unclear. Over the past 20 years, the frequency and intensity of IOD events have increased [30]. These strong IOD events have typically been observed to coincide with the ENSO in the Pacific Ocean or occur independently in the TIO, such as the extreme IOD event in 2019, which had profound impacts on the marine ecosystem. Many climate models project that climate extremes seen in 2019 are likely to occur more frequently under global warming [31]. Hence, the occurrence of these strong events provides an opportunity for studying the response processes and oceanic mechanisms of phytoplankton size structure variations to climate events.

The goal of this study is to investigate the interannual variability of phytoplankton size structure in the southern TIO based on satellite remote sensing data, specifically exploring the impact of IOD events on phytoplankton size structure. The underlying physical mechanisms influencing phytoplankton size structure during different stages of IOD events were examined.

2. Materials and Methods

2.1. Data

The data sets used in this study are described in Table 1. The mixed layer depth (MLD) from the global ocean Argo gridded data set (BOA_Argo) is defined as the depth at which the potential density has increased from that at a depth of 10 m by a threshold equivalent to the density difference for the same 0.2 °C temperature change at constant salinity. The thermocline depth is defined as the depth of the 20 °C isotherm. The nitrucline was estimated based on the 2.0 mmol m^{-3} isocline depth of nitrate from WOA18. The Niño3.4 index is calculated as SST anomalies averaged over the tropical Pacific (170°–120°W, 5°S–5°N). The dipole mode index (DMI) is defined as the difference in SST anomalies between the western (50°–70°E, 10°S–10°N) and eastern (90°–110°E, 10°–0°S) poles [32]. The surface wind stress (τ) was estimated from the bulk formula [33] $\tau = \rho_a C_D u|u|$, where ρ_a is the air density (1.2 kg m^{-3}), C_D is the drag coefficient, and $u = (u_x, u_y)$ is the surface wind. The Ekman pumping velocity (W_E) was calculated as $W_E = \frac{\nabla \times \tau}{\rho_0 f}$, where ρ_0 represents the surface density of seawater, and $f = 2\omega \cos\theta$ is the Coriolis parameter in latitude θ with the Earth rotation rate ω.

Table 1. Summary of data sets used in this study and their sources.

Variable	Data Set	Time Period	Spatial Resolution	Sources
Rrs (λ)	MODIS-Aqua L3	January 2003–December 2020	4 km, 8-day	NASA's OceanColor website https://oceandata.sci.gsfc.nasa.gov/ (accessed on 1 December 2023)
SST	NOAA OISST Version-2	January 1982–December 2020	0.25° × 0.25°, monthly	NOAA Physical Sciences Laboratory https://psl.noaa.gov/data/gridded/data.noaa.oisst.v2.html (accessed on 1 December 2023)
SSH	Ssalto/Duacs, DT merged all satellites, L4	January 2003–December 2020	0.25° × 0.25°, monthly	AVISO https://www.aviso.altimetry.fr/en/home.html (accessed on 1 December 2023)
u (u_x, u_y)	CCMP Version-3.1	January 2003–December 2020	0.25° × 0.25°, monthly	Remote Sensing Systems https://www.remss.com/measurements/ccmp/ (accessed on 1 December 2023)
Temperature, salinity, MLD	Global ocean Argo gridded data set (BOA_Argo)	January 2004–December 2020	1° × 1°, 58 standard levels within the upper 2000 m, monthly	China Argo Real-time Data Center http://www.argo.org.cn/ (accessed on 1 December 2023)
Nitrate	World Ocean Atlas 2018	Climatology	1° × 1°	NOAA National Centers for Environmental Information https://www.ncei.noaa.gov/products/ (accessed on 1 December 2023)

2.2. Estimation of Phytoplankton Size Structure

In this study, the phytoplankton size structure was detected using a CSD model [14]. The model calculates the CSD slope as an index of the phytoplankton size structure. Assuming that the CSD follows the Junge-type power law distribution, the total *Chl* and size-fractionated *Chl* (Chl_{size}) in a given diameter ranging from D_1 to D_2 can be expressed as:

$$Chl = \int_{D_{min}}^{D_{max}} Chl_0 \left(\frac{D}{D_0}\right)^{-\eta} dD \quad (1)$$

$$Chl_{size} = \int_{D_1}^{D_2} Chl_0 \left(\frac{D}{D_0}\right)^{-\eta} dD \quad (2)$$

where Chl_0 is the reference *Chl* at reference diameter D_0 (here, 0.7 μm), and η is the CSD slope. D_{min} and D_{max} were defined as 0.7 μm and 200 μm, respectively. The CSD slope was then derived as the slope of the linear regression in the log space between the inverse log-transformed median diameters, from log-transformed D_1 to D_2, and Chl_{size} normalized by the bin size. A large CSD slope represents a large fraction of smaller-sized phytoplankton, whereas a small CSD slope indicates that larger-sized phytoplankton dominate.

The model estimates the CSD slope by capturing the spectral features of the absorption coefficient of the phytoplankton ($aph(\lambda)$) with the aid of principle component analysis. The input variables of the model are remote sensing reflectance ($Rrs(\lambda)$) at eight bands (λ = 412, 443, 469, 488, 531, 547, 555, and 667 nm), which can then be converted to $aph(\lambda)$ and *Chl* to obtain the CSD slope (refer to Waga et al. [14,34] for further details). To capture the interannual variability of phytoplankton size structure, the CSD slope anomalies were computed by subtracting the corresponding monthly mean from a monthly composite. Subsequently, a band-pass filter ranging from 4 to 84 months was applied to each grid of the CSD slope anomalies to eliminate seasonal signals and long-term trends.

The use of *Chl* concentration provides adequate accuracy for global ocean applications, including oligotrophic regions, but it does not necessarily reflect the size structure of the phytoplankton communities. Conversely, the spectral shape of $aph(\lambda)$ can indicate phytoplankton size structure but often lacks accuracy in oligotrophic waters. Therefore, the primary advantage of the CSD model lies in its integration of both *Chl* and $aph(\lambda)$, allowing each variable to offset the other's limitations. This method for estimating phytoplankton size structure also effectively illustrates the spatial variations in the impacts of mesoscale eddies on phytoplankton size structure on a global scale [34].

3. Results

3.1. Climatological Mean

Figure 1 illustrates the spatial distribution of climatological surface *Chl*, CSD slope, SST, and nutricline depth seasonal cycles in the southern TIO. A smaller value for the CSD slope indicates a larger phytoplankton size structure, while a larger value for the CSD slope corresponds to a smaller phytoplankton size structure. The spatial distribution of the CSD slope in the TIO indicates that in coastal upwelling areas or in the southwestern TIO, where the thermocline and nutricline are shallow, higher *Chl* concentrations are correlated with smaller CSD slope values. Conversely, in the nutrient-depleted central equatorial Indian Ocean, lower *Chl* concentrations are associated with higher CSD slope values. The distribution characteristics of the CSD slope are consistent with other models used to estimate phytoplankton size structure [4].

Variations in phytoplankton size structure in the southern TIO are closely linked to the development of monsoons. During JJA, the southeast trades prevail in the southern TIO, and the increasing wind speed northward in the southwestern TIO within the 0°–12°S latitude range results in significant upwelling in the western TIO. This leads to a shallow nutricline (<60 m), and plentiful nutrients in this latitude band result in higher *Chl* concentrations and smaller values for the CSD slope (Figure 1c,g). Meanwhile, the southeast

winds along the Sumatra–Java region favor the generation of coastal upwelling, resulting in smaller values of CSD slope near the coast and gradually increasing values offshore, corresponding to higher *Chl* concentrations. During DJF, smaller CSD slope values or higher *Chl* concentrations are only observed in the thermocline ridge of the southwestern TIO (Figure 1a,e). During MAM and SON, significant east-west differences in CSD slope are observed, with larger values in the eastern TIO and smaller values in the western TIO. This is primarily due to a semiannual westerly wind component during the intermonsoon seasons, which transports warm water eastward, deepening the thermocline and nutricline in the eastern TIO and leading to higher SST.

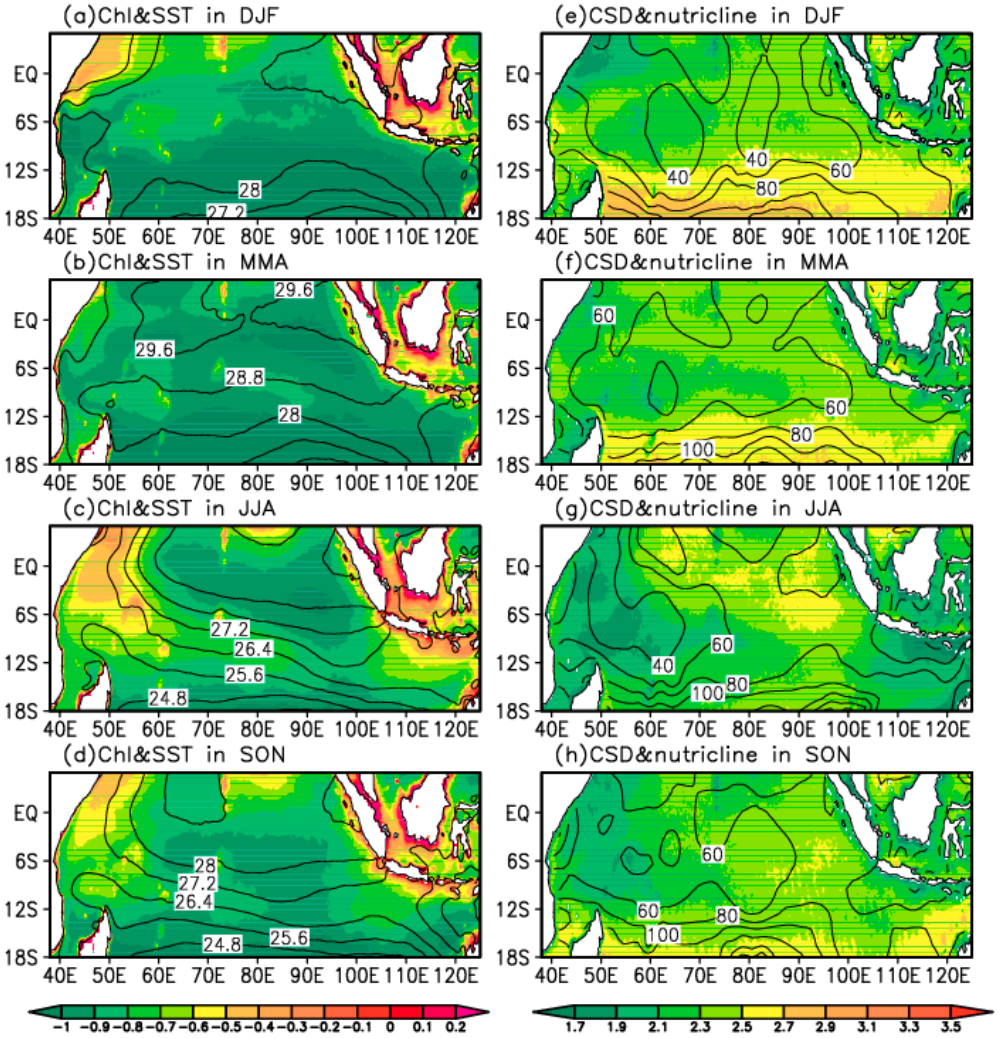

Figure 1. Climatological means for *Chl* (shading; mg/m^3) and SST (contours; °C) in (**a**) December–February, (**b**) March–May, (**c**) June–August, and (**d**) September–November. (**e**–**h**) are the same as (**a**–**d**), but for the CSD slope (shading) and nutricline depth (contours; m).

3.2. Interannual Variations in Phytoplankton Size Structure

To investigate the interannual variability in phytoplankton size structure in the southern TIO, we first computed the root mean square (RMS) of the CSD slope (Figure 2). As shown in Figure 2a, the strongest interannual variability of phytoplankton size structure occurred in the southeastern TIO and central southern TIO. In the southeastern TIO, the maximum RMS of the CSD slope appeared near the coastal areas, and the significant interannual fluctuations mainly occurred during the summer monsoon season (May to September, Figure 2b). This indicated that interannual adjustments in summertime oceanic dynamical processes had significant impacts on variations in phytoplankton size structure

in the southeastern TIO. In the central southern TIO, the strongest interannual CSD slope fluctuations occurred at 70°–90°E, 5°–15°S. Moreover, the maximum interannual RMS of the CSD slope mainly occurred from January to July in the central southern TIO.

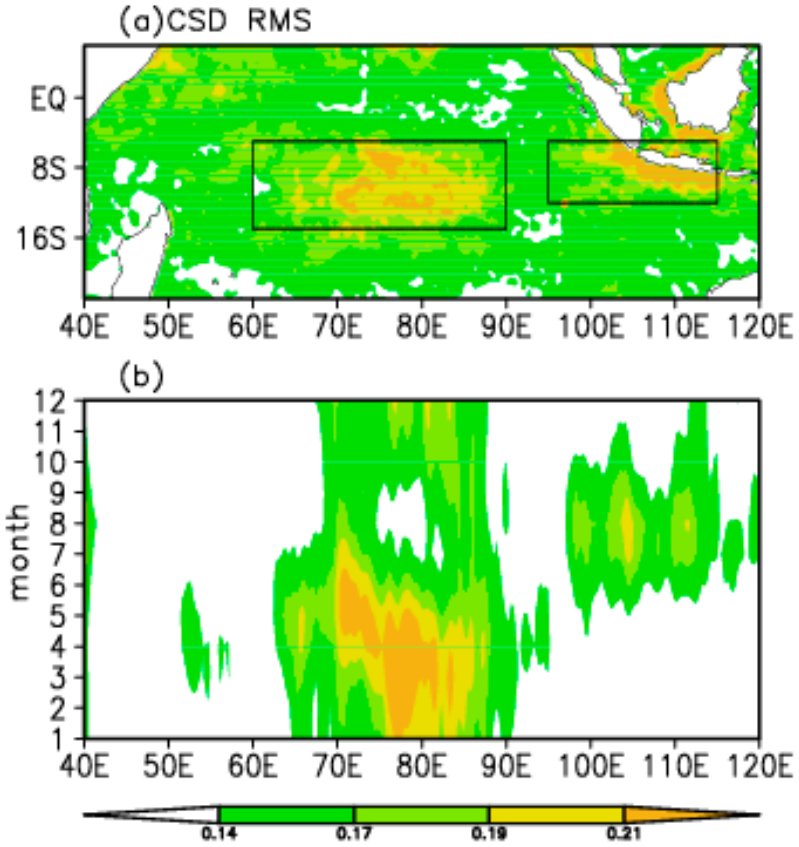

Figure 2. (**a**) RMS variance distribution of CSD slope interannual anomalies during the period of 2003–2020. (**b**) Longitude–time sections of CSD slope RMS averaged meridionally over 8°–12°S. The anomaly is calculated relative to the climatological seasonal cycle based on the years 2003–2020.

The time series of CSD slope and *Chl* anomalies in the southeastern TIO and the central southern TIO is presented in Figure 3. Both CSD slope and *Chl* anomalies exhibited pronounced interannual variability, with a strong negative correlation between them (Figure 3b,c). Negative CSD slope anomalies indicated a larger proportion of large-sized phytoplankton in this region compared to the climatological CSD slope, while positive CSD slope anomalies suggested the prevalence of small-sized phytoplankton. The interannual variability of *Chl* was more pronounced in the southeastern TIO than in the central southern TIO, yet the interannual variability of CSD slope was comparable between the two regions. The interannual fluctuations in the CSD slope in the southeastern TIO were sensitive to the IOD events, showing a negative correlation with a correlation coefficient of 0.66 (Figure 4a). The negative CSD slope anomalies and elevated *Chl* in the southeastern TIO were associated with positive IOD events, while the positive CSD slope anomalies and a decrease in *Chl* were linked to the negative IOD events (Figure 3b). In contrast, changes in CSD slope anomalies in the central southern TIO were positively correlated with the IOD (Figure 4b). Although the correlation coefficient was not very high (R = 0.35, Figure 4d), the CSD slope anomalies responded pronounced to strong IOD events or years when both IOD and ENSO occurred simultaneously (Figure 3a,c). During strong negative IOD events, the central southern TIO was dominated by larger-sized phytoplankton communities, while smaller-sized phytoplankton structures were favored during positive IOD events. The scatter diagrams demonstrate the strong relationship between CSD slope anomalies and thermocline depth and SSTA (Figure 4). The contrasting responses of phytoplankton

size structure to the IOD in these two regions highlights the distinct influence of varying oceanic processes.

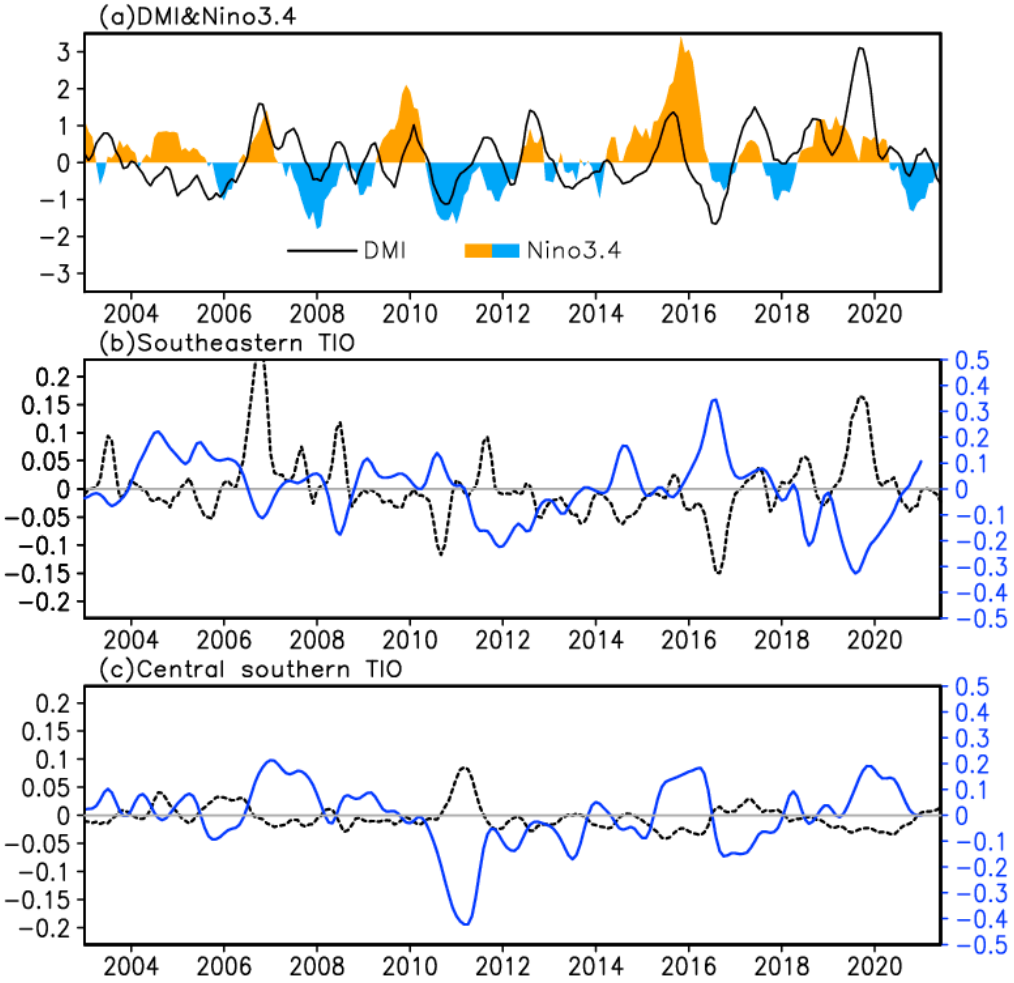

Figure 3. (**a**) Time series of the Niño3.4 index (shading) and the dipole mode index (DMI, black curve) and (**b**,**c**) CSD slope anomalies (blue curve) and *Chl* anomalies (black dashed curve) averaged over the southeastern TIO (black box in Figure 2a; 95°–115°E, 5°–12°S) and the central southern TIO (black box in Figure 2a; 60°–90°E, 5°–15°S), respectively.

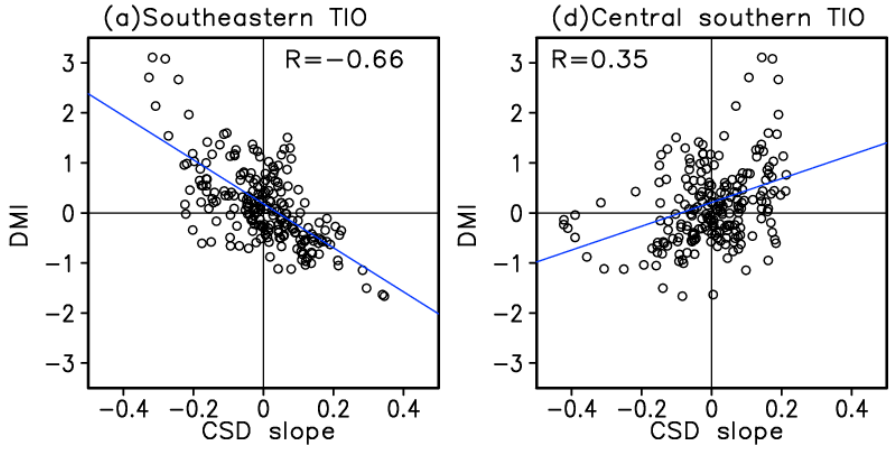

Figure 4. *Cont.*

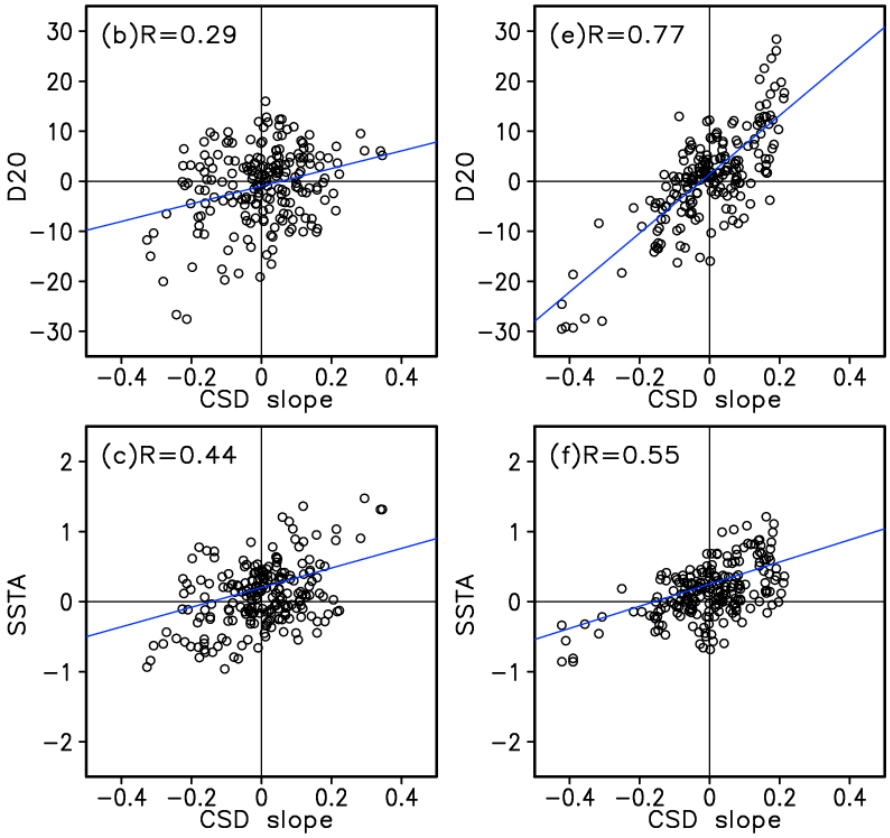

Figure 4. Scatter diagrams of CSD slope anomalies against (**a**) DMI, (**b**) thermocline depth anomalies (D20, cm), and (**c**) SSTA (°C) in the Southeastern TIO (black box in Figure 2a; 95°–115°E, 5°–12°S). (**d**–**f**) are the same as (**a**–**c**) but for the central southern TIO (black box in Figure 2a; 60°–90°E, 5°–15°S).

3.3. Features in IOD Events

During the period from 2003 to 2020, three strong positive IOD events occurred in 2006, 2015, and 2019, and three strong negative IOD events occurred in 2005, 2010, and 2016 (Figure 3a). The negative IOD event in 2010 occurred concurrently with the extreme La Niña in the tropical Pacific Ocean, while the positive IOD event in 2015 coincided with the extreme El Niño, and the IOD event in 2019 was the strongest event occurring independently without El Niño since the 1960s [21]. Figure 5 presents longitude–time sections of the CSD slope anomalies for the three strong positive and three strong negative IOD events. The IOD exhibits seasonal phase-locking characteristics, developing from late spring to early summer, strengthening in summer, peaking in autumn, and gradually diminishing in winter [35]. The variations in CSD slope anomalies in the southeastern TIO were generally consistent with the evolution process of the IOD (Figure 5). These variations exhibited a positive correlation with SSTA and thermocline depth anomalies (Figure 4b,c). During positive IOD events, significant negative CSD slope anomalies were observed when the southeastern TIO was characterized by SST cooling (Figure 6d,e). The composite of the CSD slope revealed that the negative anomalies occurred in April–May and continued to develop during JJA (Figure 5d–f). The phytoplankton size structure shifts toward smaller sizes extending from nearshore areas to offshore regions (Figure 7a). The maximum negative CSD slope anomalies appeared in SON, and they rapidly dissipated in DJF (Figure 7a–e). Compared to positive IOD events, the negative IOD events led to a deepening of the thermocline or SST warming, resulting in positive CSD slope anomalies over a larger area, dominated by smaller phytoplankton communities in the southeastern TIO. The positive CSD slope anomalies peaked in JJA and gradually dissipated in SON during negative IOD events (Figure 8a–e).

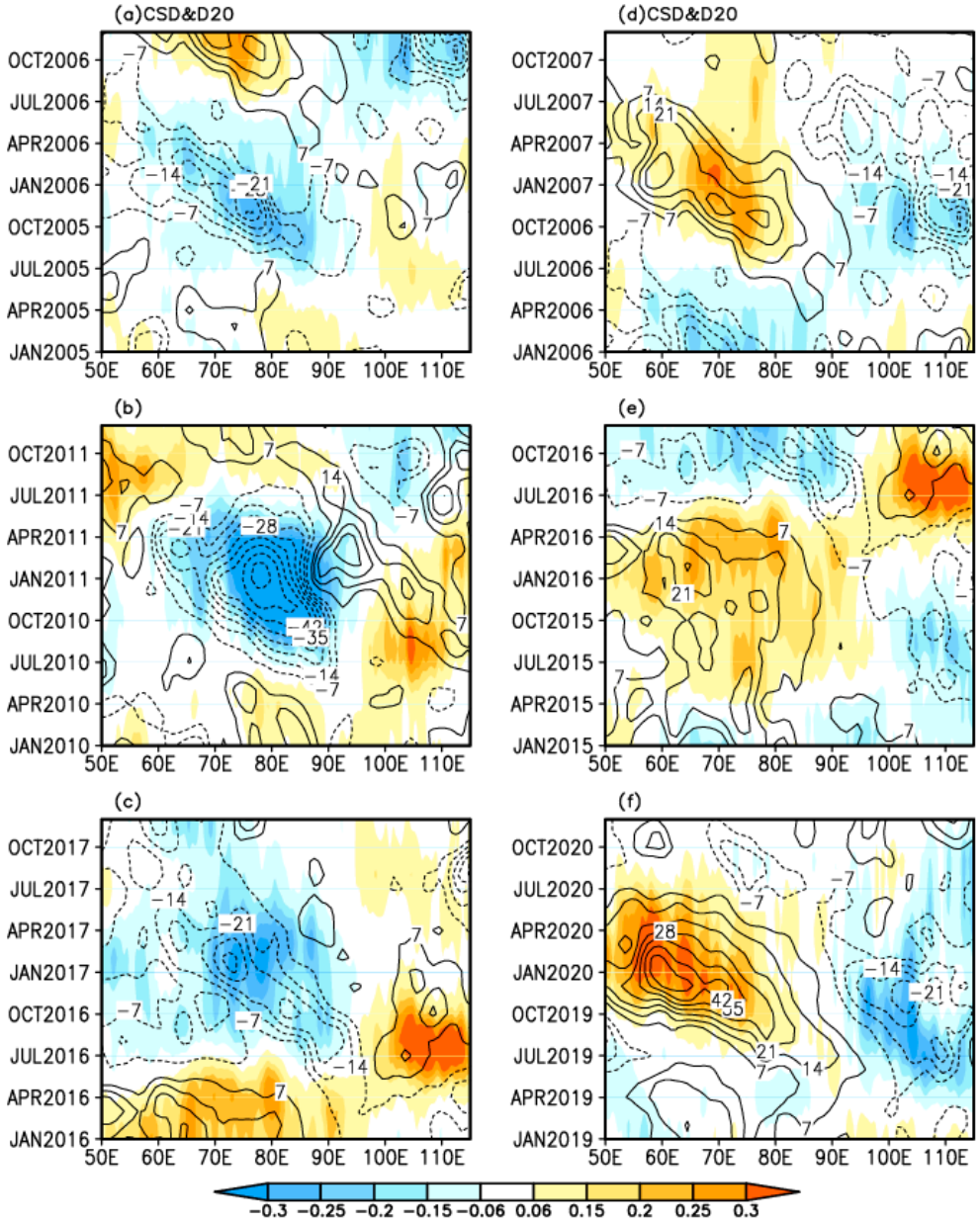

Figure 5. Longitude–time sections of (**a**–**c**) CSD slope (shading) and thermocline depth (contours; cm; Contour interval is 7 cm.) anomalies averaged between 8°S and 12°S for the strong positive IOD events (2006, 2015, and 2019). (**d**–**f**) are the same as (**a**–**c**) but for the strong negative IOD events (2005, 2010, and 2016).

Under the influence of the IOD, the phytoplankton size structure in the central southern TIO exhibited significant changes, characterized by wider extent, greater magnitude, and longer duration. The CSD slope anomalies in the central southern TIO emerged in late spring to early summer and persisted until the following spring, and the abnormal changes in phytoplankton size structure propagated westward with the development of the IOD (Figure 5). Significant positive CSD slope anomalies occurred during the decay phase (DJF) of the positive IOD, with the maximum values appearing in the southwestern TIO where the thermocline was shallow (Figure 7). Conversely, the central southern TIO was dominated by larger-sized phytoplankton communities during negative IOD events (Figure 5a–c). The negative CSD slope anomalies peaked in DJF, displaying noticeable features of westward and southward propagation (Figure 8). However, the maximum of negative CSD slope anomalies predominantly manifested between 70–90°E, indicating

pronounced asymmetry in the spatial response of phytoplankton size structure to IOD events in the southern TIO (Figure 8a–e).

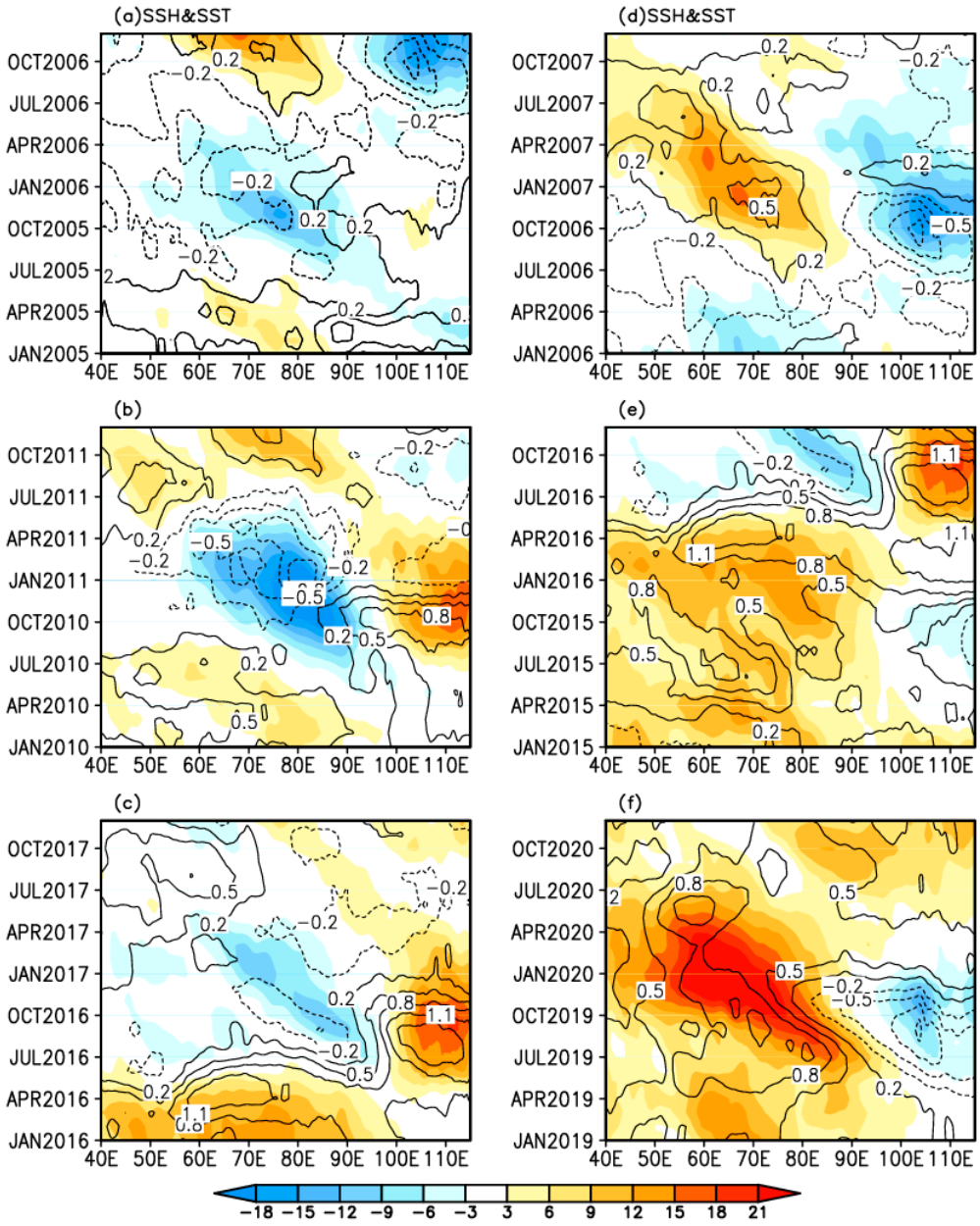

Figure 6. Longitude–time sections of (**a**–**c**) SSH anomalies (shading; cm; Contour interval is 7 cm). And SST anomalies (contours; °C) averaged between 8°S and 12°S for the strong positive IOD events (2006, 2015, and 2019). (**d**–**f**) are the same as (**a**–**c**) but for the strong negative IOD events (2005, 2010, and 2016).

Additionally, the magnitude and spatial pattern of phytoplankton size structure varied among different IOD events. During the extreme positive IOD event in 2019, the most significant variations in phytoplankton size structure were observed in the southern TIO. Significant negative CSD slope anomalies were evident in the southeastern TIO, while noticeable positive anomalies were observed in the western TIO. The 2015 positive IOD event, concurrent with the extreme 2015/2016 El Niño, had a more extensive and longer-lasting impact on phytoplankton size structure in the southern TIO. However, the magnitude of CSD slope anomalies was smaller compared to those in 2019. The negative IOD event in 2010, coinciding with an extreme La Niña event, resulted in significant

negative CSD slope anomalies in the central TIO, dominated by larger-sized phytoplankton communities. These results indicate that the response of phytoplankton size structure to IOD events depends on the amplitude and duration of the IOD, as well as the intensity of concurrent ENSO events.

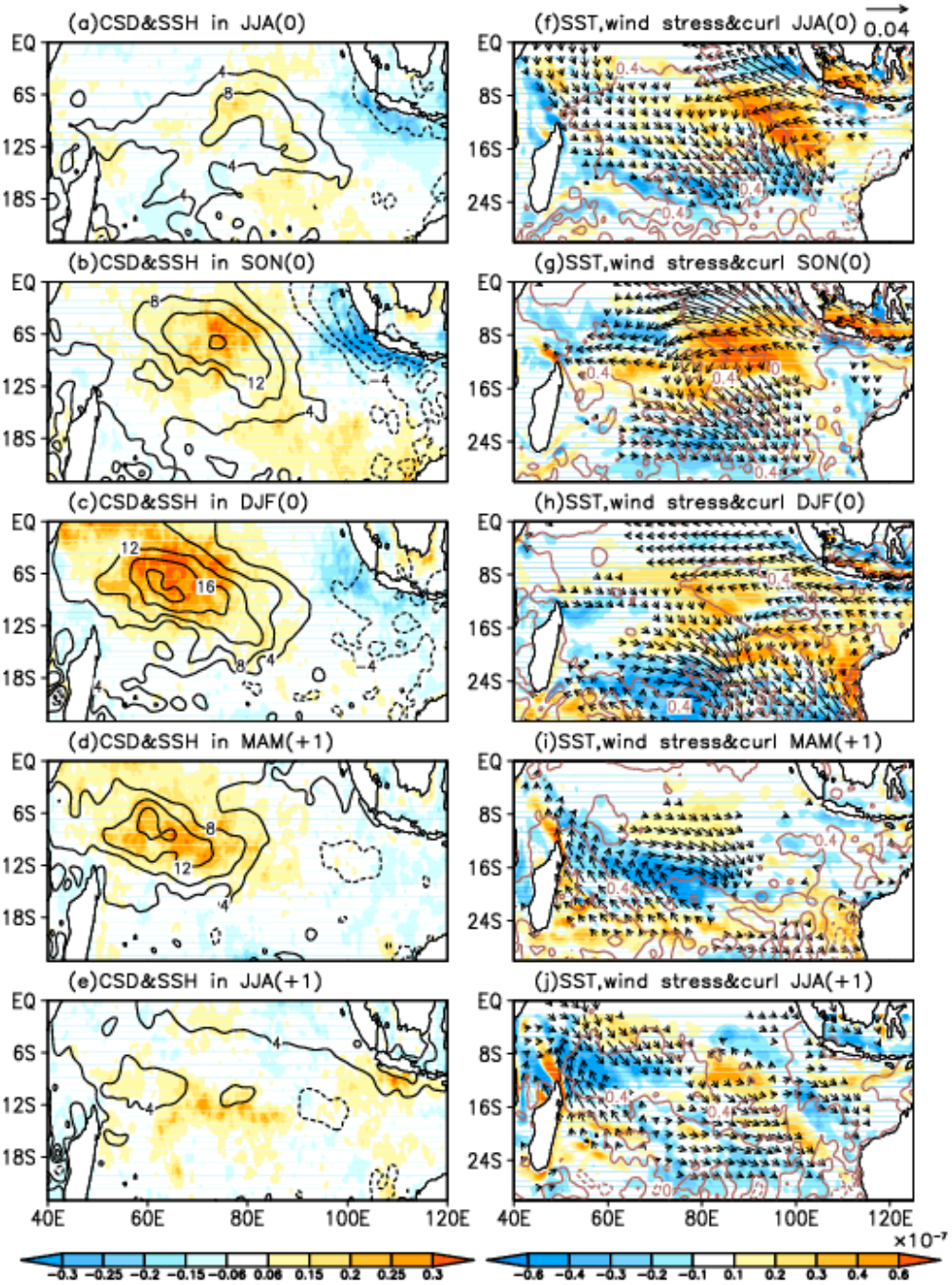

Figure 7. Composite evolutions of CSD slope (shading) and SSH (contours; cm) anomalies for (**a**) June–August (0), (**b**) September–November (0), (**c**) December–February (0), (**d**) March–May (+1), and (**e**) June–August (+1) for the positive IOD events. (0) and (+1) represent seasons during the IOD peak year and those after the peak year, respectively. (**f**–**j**) are the same as (**a**–**e**) but for SST (contours; °C), wind stress (vectors; N/m^2), and wind stress curl (shading; N/m^3) anomalies.

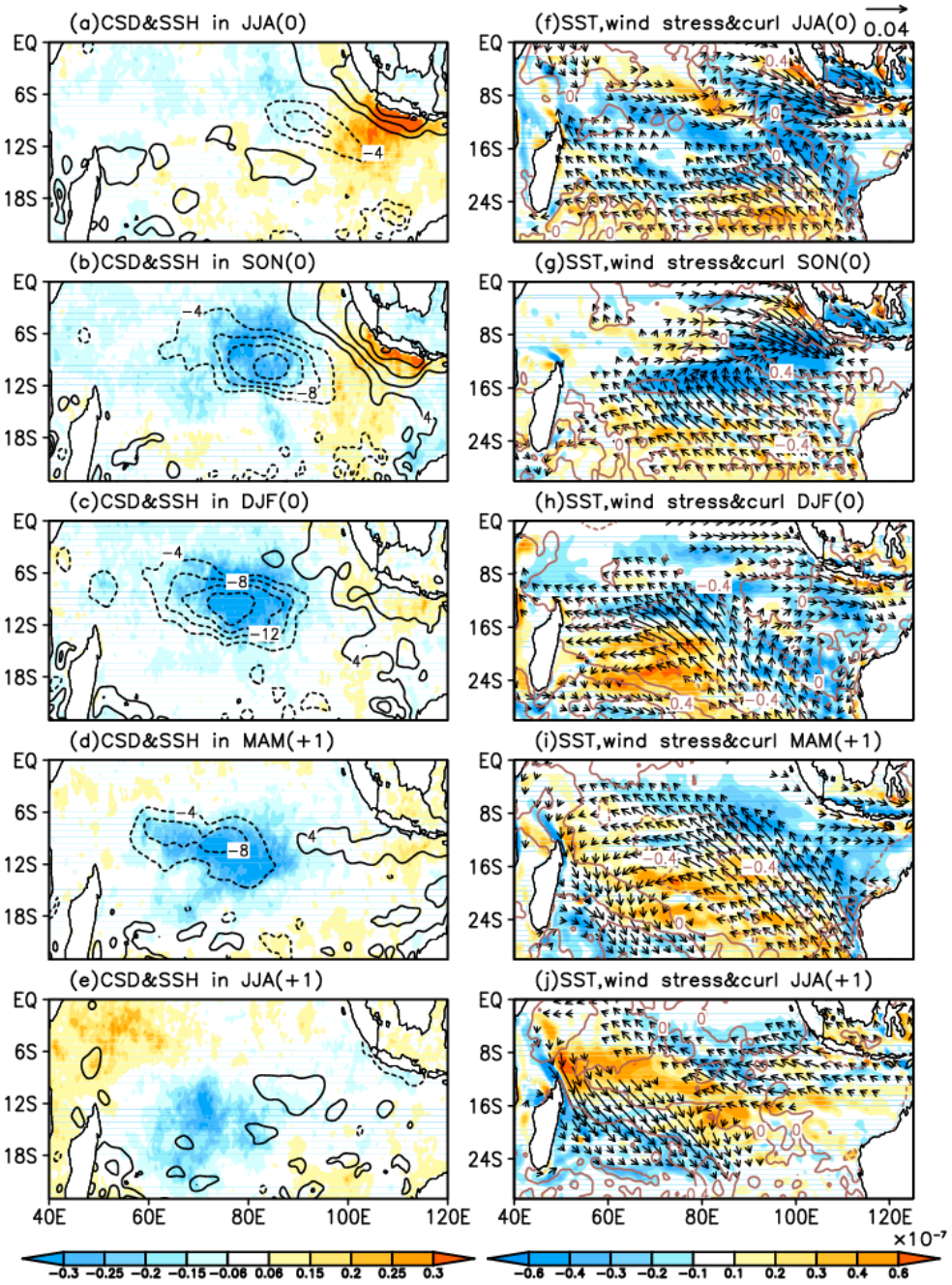

Figure 8. Composite evolutions of CSD slope (shading) and SSH (contours; cm) anomalies for (**a**) June–August (0), (**b**) September–November (0), (**c**) December–February (0), (**d**) March–May (+1), and (**e**) June–August (+1) for the negative IOD events. (0) and (+1) represent seasons during the IOD peak year and those after the peak year, respectively. (**f**–**j**) are the same as (**a**–**e**) but for SST (contours; °C), wind stress (vectors; N/m^2), and wind stress curl (shading; N/m^3) anomalies.

3.4. Physical Processes

Phytoplankton growth in the tropics is limited by nutrient availability despite abundant light. In the preceding section, a significant relationship was observed between interannual variations in phytoplankton size structure and IOD. The longitude–time sections of thermocline depth anomalies further indicate a close correspondence between phytoplankton size structure and the thermocline depth in the southern TIO (Figure 5). This suggests that oceanic dynamic processes linked to the IOD modulate nutrient distribution in the southern TIO by affecting the thermocline, thereby directly influencing

phytoplankton size structure variability. The following sections elaborate on the physical mechanisms underlying variations in phytoplankton size structure in the southeastern TIO and the central southern TIO.

3.4.1. Southeastern TIO

During the summer monsoon season, the southeastern wind induces the upwelling of cool, nutrient-rich water to the surface, thereby promoting phytoplankton growth in the southeastern TIO [20]. During positive IOD events, the southeast wind anomalies in the southeastern TIO strengthened the Ekman transport, and the nearshore negative wind stress curl anomalies also indicated intensified offshore Ekman pumping. This enhanced upwelling resulted in a shallower thermocline and SST cooling, which consistently enhanced the nutrient supply in the upper ocean (Figures 5 and 7f). Negative CSD slope anomalies in the nearshore regions of the southeastern TIO indicated a shift in the size structure of phytoplankton communities toward larger size during JJA (Figure 7a). The persistent strengthening of southeast wind anomalies further intensified the upwelling process during the mature phase of the positive IOD events (Figure 7b,g). The offshore anomalous anticyclonic circulation further facilitated the expansion of larger sizes of phytoplankton toward the equator and offshore regions, coinciding with the most significant negative CSD slope anomalies. The distribution characteristics of phytoplankton size structure were likely related to horizontal advection induced by the enhanced westward-flowing South Equatorial Current during positive IOD events [26,36].

Conversely, the northwest wind anomalies during the negative IOD events reduced coastal upwelling, resulting in a deepening of the thermocline, increased SSH, and warming SST in the southeastern TIO (Figure 8f,g). This led to a reduced nutrient supply to the surface layer, thereby inhibiting the growth of phytoplankton and causing the size structure of phytoplankton communities to shift toward smaller size (Figure 8a,b). The maximum positive CSD slope anomalies occurred in the developing phase of the negative IOD events when the phytoplankton communities were dominated by smaller-sized phytoplankton (Figure 8a). The significant positive CSD slope anomalies were observed further southward off the coast of Java, influenced by the offshore anomalous cyclonic circulation. During the mature phase (SON) of negative IOD events, although SSH, SST, and thermocline depth anomalies reached their peak values, the magnitude of positive CSD slope anomalies was smaller than those observed in JJA.

3.4.2. Central Southern TIO

The most prominent characteristic of phytoplankton size structure variations during IOD events in the central southern TIO was the evident westward propagation. The response of phytoplankton size structure indicated the influence of oceanic Rossby waves. Previous research has demonstrated the impact of wind-induced Ekman pumping and Rossby wave dynamics on the thermocline depth within the southern region of the southern TIO.

During the early stages of positive IOD events, anomalous anticyclonic circulation in the southeastern TIO led to the convergence of warm waters and triggered westward-propagating downwelling Rossby waves. However, the changes in phytoplankton size structure in the southern TIO were not significant during this period (Figure 5d–f). During JJA, the anomalous anticyclonic circulation intensified, contributing to an increase in the MLD (Figure 9a). Simultaneously, downwelling Rossby waves further deepened the thermocline, causing warming in the subsurface with temperature anomalies exceeding 0.8 °C observed at depths ranging from 60 to 80 m (Figure 9a). These processes impeded the vertical transport of nutrients to the upper ocean layers. The phytoplankton size structure adjustments were observed within regions exhibiting maximum positive SSH anomalies, indicating a transition toward smaller size in phytoplankton communities.

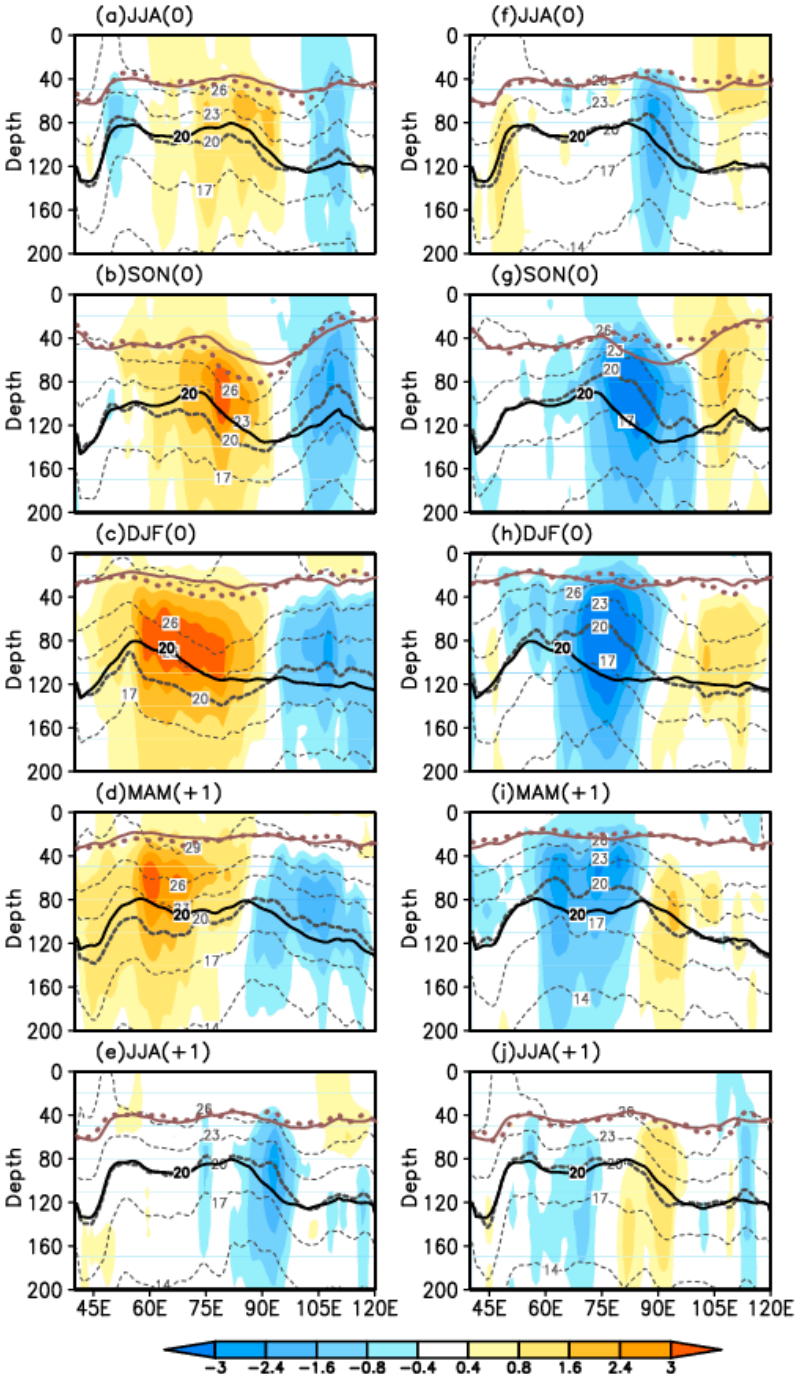

Figure 9. Composite depth–longitude sections of temperature anomalies (shading; °C), superimposed on mean temperature (dashed contours) for (**a**) June–August (0), (**b**) September–November (0), (**c**) December–February (0), (**d**) March–May (+1), and (**e**) June–August (+1) for the positive IOD events. The black thick curves in (**a**–**e**) represent climatological D20 (m) for the corresponding months. The pink thick and dotted curves in (**a**–**e**) represent the MLD (m) for the corresponding months and the climatology, respectively. (**f**–**j**) The same as (**a**–**e**) but for the composite evolutions of the negative IOD events. All variables are averaged meridionally over 8°–12°S.

During SON, the anticyclonic circulation intensified further, extending the influence of positive wind stress curl anomalies into the central southern TIO. This further strengthened the westward-propagation downwelling Rossby waves. As a consequence, there was a notable deepening of MLD (>30 m) and a more pronounced warming of subsurface temperatures (>2.4 °C). These processes further reduced nutrient transport into the euphotic

zone, thus constraining phytoplankton growth. The positive CSD slope anomalies were more evident in the central southern TIO. Although the surface wind weakened during DJF, the downwelling Rossby waves and the associated thermocline variations reached their peak (Figure 9c). Subsurface warming occurred in the southwestern TIO thermocline ridge region, increasing by over 3 °C, resulting in the strongest response of phytoplankton size structure to smaller cell sizes across the entire southwestern TIO (Figure 7c).

During the following MAM, the influence of Rossby waves diminished, leading to a weakening of subsurface temperature warming. However, the SST warming persisted, leading to significant positive CSD slope anomalies.

Compared to positive IOD events, the response of phytoplankton size structure and ocean dynamics during negative IOD events displays inverse patterns. During the development phase of negative IOD events, anomalous cyclonic wind patterns in the southeastern TIO induced negative wind stress curl and subsequent Ekman upwelling (Figure 8f,j). This process uplifted the MLD and thermocline, initiating the westward propagation of upwelling Rossby waves. Subsurface temperature cooling also exhibited westward propagation, consistent with variations in SSH and thermocline depth (Figure 9f,j). During the mature and decaying phase of negative IOD events, the thermocline was uplifted more than 50 m, facilitating the transport of nutrients to the surface through intensified upwelling (Figure 9g,h). This nutrient enrichment promoted the growth of larger-sized phytoplankton communities. Larger-sized phytoplankton communities propagate westward and southward under the influence of upwelling Rossby waves (Figure 8a–e).

4. Discussion

The satellite-derived phytoplankton size structure in the southern TIO exhibited distinct seasonal and interannual variations. At the interannual scale, the changes in phytoplankton size structure in the southeastern TIO were very sensitive to the IOD events. During positive (negative) IOD events, the intensification of southeastern wind anomalies and coastal upwelling favored a greater dominance of larger (smaller) size phytoplankton communities. These findings aligned with the analysis conducted by Brewin et al. [2], who employed a three-component model to estimate phytoplankton size structure from satellite observations. Their results demonstrated a negative correlation between interannual fluctuations in the proportion of nano- and micro-phytoplankton relative to total *Chl* and changes in SST, SSH, and stratification in the TIO, whereas variations in the proportion of pico-phytoplankton exhibited a positive correlation with these physical variables. The model proposed by Brewin et al. [2] assumes a change in phytoplankton size structure with a change in *Chl*. Other methods based on phytoplankton absorption spectral characteristics [12] or backscattering approaches [4] for retrieving phytoplankton size structure also exhibit a close relationship with *Chl* [5]. These interrelationships suggest that alternative approaches are likely to reach similar conclusions as the CSD model. Additionally, the interannual variability of *Chl* concentrations in the relatively nutrient-depleted central southern TIO was smaller compared to that in the southeastern TIO. However, the interannual variability of phytoplankton size structure remained significant, comparable to that in the southeastern TIO (Figure 3). This suggests that phytoplankton size structure can serve as a useful indicator for assessing phytoplankton response to climate change.

In the central southern TIO, the modulation of the thermocline induced by the IOD resulted in significant variations in phytoplankton size structure. These results highlight the close connection between variations in marine phytoplankton size structure and ocean dynamic processes. Several studies have indicated that the wind stress curl over the interior TIO is the main driver of the interannual variability in SSH and thermocline depth in the southern TIO [28,37]. The longitude–time sections of wind stress curl and Ekman upwelling velocity anomalies in Figure 10 further demonstrate that local wind forcing modulates the thermocline depth in the Southeastern TIO and triggers the oceanic Rossby waves. Both local wind forcing and oceanic Rossby waves exert substantial influence on

the phytoplankton size structure in the central southern TIO from the development to the maturity of the IOD events. Previous studies found that downwelling oceanic Rossby waves associated with the anomalous anticyclonic wind stress curls in the southeast TIO deepen the thermocline and warm the subsurface in the southwestern TIO [35]. Our study also revealed that Rossby waves persisted in modulating the variations in phytoplankton size structure during IOD events. Notably, during the decay phase of the extreme positive IOD events in 2019 or the strong IOD event in 2015, the anomalous phytoplankton size structure persisted into the following spring. This was primarily attributed to ocean–atmosphere interactions associated with the sustained warming in the southwestern TIO induced by Rossby waves during extreme positive IOD events in 2019 or the strong IOD event in 2015. Such SST warming triggered cross-equatorial "C-shaped" wind anomalies, leading to basin-wide warming via wind-evaporation-SST feedback [35,38]. Therefore, the sustained SST warming kept the upper ocean consistently lacking in nutrients. This hindered the growth of larger-sized phytoplankton, contributing to the presence of negative CSD slope anomalies until the end of the subsequent spring or early summer (Figure 4d–f).

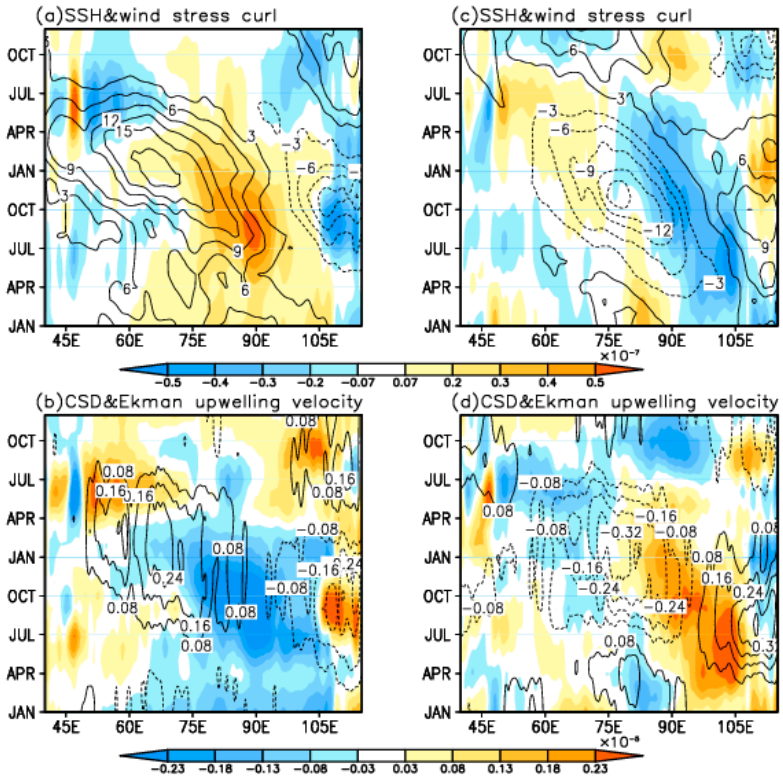

Figure 10. Composite longitude–time sections of (**a**) wind stress curl (shading; N/m^3) and SSH (contours; cm; Contour interval is 3 cm.) and (**b**) Ekman upwelling velocity (shading; m/s) and CSD slope (contours; Contour interval is 0.08.) anomalies averaged meridionally over 8°–10°S for the positive IOD events. (**c**,**d**) The same as (**a**,**b**) but for the negative IOD events.

In this study, we recognized a significant influence of the IOD on phytoplankton size structure, highlighting discernible differences in the effects across various IOD events. Under the influence of the extreme positive IOD event, the southwestern TIO experienced a subsurface temperature increase exceeding 3 °C, resulting in the most significant variability in phytoplankton size structure. Utilization of a three-dimensional ocean biogeochemistry model assimilating ocean color data, Arteaga and Rousseaux [15] observed a significant decline of approximately 40% in surface *Chl* concentrations during the extreme warmth of the 2016 El Niño event, accompanied by an almost complete collapse of diatoms. The abnormal SST warming also led to dramatic changes in phytoplankton communities in the northeast Pacific Ocean, triggering widespread toxic algae blooms that caused devastating

ecological damage. Recent studies have suggested an increased frequency of events resembling the positive IOD event of 2019 in the context of global warming [31]. Therefore, these results suggest that the increased frequency of positive IOD events will lead to a trend toward a smaller size structure in the western TIO, potentially impacting energy transfer within the food chain or the downward export of carbon.

5. Conclusions

Using remotely sensed phytoplankton size structure data, we investigated the interannual variations in phytoplankton size structure in the southern TIO and associated physical mechanisms. The strongest interannual fluctuations in phytoplankton size structure occurred in the southeastern TIO and central southern TIO and were very sensitive to IOD events.

In the southeastern TIO, the southeast wind anomalies reinforced coastal upwelling off Java and Sumatra during positive IOD events, leading to a shift toward larger phytoplankton communities. The most pronounced variations in phytoplankton size structure were observed during the positive IOD's development phase (JJA). Conversely, the anomalous northwest wind during negative IOD events dampened coastal upwelling, favoring smaller phytoplankton communities, with significant changes observed during the mature phase (SON) of the IOD.

In the central southern TIO, one of the most prominent phenomena observed during IOD events is the clear westward propagation of phytoplankton size structure variations. Both local wind forcing and oceanic Rossby waves have a significant impact on the interannual variations of phytoplankton size structure. During positive (negative) IOD events, the anomalous anticyclonic (cyclonic) circulation generated positive (negative) wind stress curl anomalies and triggered the westward propagation of downwelling (upwelling) Rossby waves. These processes deepened (uplifted) the thermocline, causing subsurface warming (cooling) and suppressing (enhancing) nutrient transport to the surface. Consequently, smaller (larger) phytoplankton cells dominated in the central southern TIO. During positive IOD events, the most significant fluctuations in phytoplankton size structure were observed in the thermocline ridge region, whereas during negative IOD events, these variations occurred in the central southern TIO east of 60°. Moreover, during the concurrent positive IOD and El Niño event in 2015 or the extreme positive IOD event in 2019, sustained warming in the southwestern TIO induced basin-wide warming in the subsequent spring, resulting in a continued dominance of small-sized phytoplankton communities in the western TIO. Our results underscore the influence of climate event-related oceanic dynamic processes on phytoplankton size structure. These findings deepen our understanding of how phytoplankton respond to climate events, with significant implications for ecosystem changes in a warming climate.

Author Contributions: Conceptualization, X.L. and L.M.; data curation, Y.L. and Q.N.; formal analysis, X.L. and W.Z.; funding acquisition, Y.L. and L.M.; investigation, X.L.; methodology, X.L., Y.L., W.Z. and L.M.; project administration, L.M.; resources, Y.L.; software, W.Z. and Q.N.; supervision, L.M.; Validation, X.L., Y.L. and Q.N.; writing—original draft, X.L., Y.L. and W.Z.; writing—review and editing, X.L., Y.L., Q.N. and L.M. All authors have read and agreed to the published version of the manuscript.

Funding: This work is supported by the Natural Science Foundation of China (grant number 42170617, 42106169), the Shenzhen Science and Technology Program (grant No. KCXFZ20211020164015024) and the Research Team Cultivation Program of Shenzhen University (grant No. 2023JCT002).

Data Availability Statement: The original contributions presented in the study are included in the article, and further inquiries can be directed to the corresponding author.

Conflicts of Interest: The authors declare that the research was conducted in the absence of any commercial or financial relationships that could be construed as a potential conflict of interest.

References

1. Sieburth, J.M.; Smetacek, V.; Lenz, J.J.L. Pelagic ecosystem structure: Heterotrophic compartments of the plankton and their relationship to plankton size fractions 1. *Limnol. Oceanogr.* **1978**, *23*, 1256–1263. [CrossRef]
2. Brewin, R.J.W.; Hirata, T.; Hardman-Mountford, N.J.; Lavender, S.J.; Sathyendranath, S.; Barlow, R. The influence of the Indian Ocean Dipole on interannual variations in phytoplankton size structure as revealed by Earth Observation. *Deep-Sea Res. Part II-Top. Stud. Oceanogr.* **2012**, *77–80*, 117–127. [CrossRef]
3. IOCCG. Phytoplankton functional types from Space. In *Reports of the International Ocean-Colour Coordinating Group (IOCCG); 15*; Sathyendranath, S., Ed.; International Ocean-Colour Coordinating Group: Petersburg, FL, USA, 2014; pp. 1–156.
4. Kostadinov, T.S.; Siegel, D.A.; Maritorena, S. Retrieval of the particle size distribution from satellite ocean color observations. *J. Geophys. Res.-Ocean.* **2009**, *114*, C9. [CrossRef]
5. Mouw, C.B.; Hardman-Mountford, N.J.; Alvain, S.; Bracher, A.; Brewin, R.J.W.; Bricaud, A.; Ciotti, A.M.; Devred, E.; Fujiwara, A.; Hirata, T.; et al. A Consumer's Guide to Satellite Remote Sensing of Multiple Phytoplankton Groups in the Global Ocean. *Front. Mar. Sci.* **2017**, *4*, 41. [CrossRef]
6. Brewin, R.J.W.; Hardman-Mountford, N.J.; Lavender, S.J.; Raitsos, D.E.; Hirata, T.; Uitz, J.; Devred, E.; Bricaud, A.; Ciotti, A.; Gentili, B. An intercomparison of bio-optical techniques for detecting dominant phytoplankton size class from satellite remote sensing. *Remote Sens. Environ.* **2011**, *115*, 325–339. [CrossRef]
7. Mousing, E.A.; Ellegaard, M.; Richardson, K. Global patterns in phytoplankton community size structure-evidence for a direct temperature effect. *Mar. Ecol. Prog. Ser.* **2014**, *497*, 25–38. [CrossRef]
8. Siegel, D.A.; DeVries, T.; Cetinic, I.; Bisson, K.M. Quantifying the Ocean's Biological Pump and Its Carbon Cycle Impacts on Global Scales. *Annu. Rev. Mar. Sci.* **2023**, *15*, 329–356. [CrossRef] [PubMed]
9. Uitz, J.; Claustre, H.; Morel, A.; Hooker, S.B. Vertical distribution of phytoplankton communities in open ocean: An assessment based on surface chlorophyll. *J. Geophys. Res.-Ocean.* **2006**, *111*, C8. [CrossRef]
10. Hirata, T.; Hardman-Mountford, N.J.; Brewin, R.J.W.; Aiken, J.; Barlow, R.; Suzuki, K.; Isada, T.; Howell, E.; Hashioka, T.; Noguchi-Aita, M.; et al. Synoptic relationships between surface Chlorophyll-*a* and diagnostic pigments specific to phytoplankton functional types. *Biogeosciences* **2011**, *8*, 311–327. [CrossRef]
11. Mouw, C.B.; Yoder, J.A. Optical determination of phytoplankton size composition from global SeaWiFS imagery. *J. Geophys. Res.-Ocean.* **2010**, *115*, C12. [CrossRef]
12. Ciotti, A.M.; Lewis, M.R.; Cullen, J.J. Assessment of the relationships between dominant cell size in natural phytoplankton communities and the spectral shape of the absorption coefficient. *Limnol. Oceanogr.* **2002**, *47*, 404–417. [CrossRef]
13. Roy, S.; Sathyendranath, S.; Bouman, H.; Platt, T. The global distribution of phytoplankton size spectrum and size classes from their light-absorption spectra derived from satellite data. *Remote Sens. Environ.* **2013**, *139*, 185–197. [CrossRef]
14. Waga, H.; Hirawake, T.; Fujiwara, A.; Kikuchi, T.; Nishino, S.; Suzuki, K.; Takao, S.; Saitoh, S.I. Differences in Rate and Direction of Shifts between Phytoplankton Size Structure and Sea Surface Temperature. *Remote Sens.* **2017**, *9*, 222. [CrossRef]
15. Arteaga, L.A.; Rousseaux, C.S. Impact of Pacific Ocean heatwaves on phytoplankton community composition. *Commun. Biol.* **2023**, *6*, 263. [CrossRef]
16. Chiba, S.; Batten, S.; Sasaoka, K.; Sasai, Y.; Sugisaki, H. Influence of the Pacific Decadal Oscillation on phytoplankton phenology and community structure in the western North Pacific. *Geophys. Res. Lett.* **2012**, *39*, 15. [CrossRef]
17. Barton, A.D.; Irwin, A.J.; Finkel, Z.V.; Stock, C.A. Anthropogenic climate change drives shift and shuffle in North Atlantic phytoplankton communities. *Proc. Natl. Acad. Sci. USA* **2016**, *113*, 2964–2969. [CrossRef] [PubMed]
18. Hermes, J.C.; Reason, C.J.C. Annual cycle of the South Indian Ocean (Seychelles-Chagos) thermocline ridge in a regional ocean model. *J. Geophys. Res.-Ocean.* **2008**, *113*, C4. [CrossRef]
19. Hood, R.R.; Beckley, L.E.; Wiggert, J.D. Biogeochemical and ecological impacts of boundary currents in the Indian Ocean. *Prog. Oceanogr.* **2017**, *156*, 290–325. [CrossRef]
20. McCreary, J.; Murtugudde, R.; Vialard, J.; Vinayachandran, P.; Wiggert, J.D.; Hood, R.R.; Shankar, D.; Shetye, S.R. Biophysical processes in the Indian Ocean. *Indian Ocean. Biogeochem. Process. Ecol. Var.* **2009**, *185*, 9–32.
21. Du, Y.; Zhang, Y.H.; Zhang, L.Y.; Tozuka, T.; Ng, B.M.; Cai, W.J. Thermocline Warming Induced Extreme Indian Ocean Dipole in 2019. *Geophys. Res. Lett.* **2020**, *47*, e2020GL090079. [CrossRef]
22. Currie, J.C.; Lengaigne, M.; Vialard, J.; Kaplan, D.M.; Aumont, O.; Naqvi, S.W.A.; Maury, O. Indian Ocean Dipole and El Nino/Southern Oscillation impacts on regional chlorophyll anomalies in the Indian Ocean. *Biogeosciences* **2013**, *10*, 6677–6698. [CrossRef]
23. Li, H.L.; Zhang, J.J.; Wang, X.Y.; Zhu, Y.L.; Liu, L.; Wang, B.D.; Zhang, X.L.; Wei, Q.S.; Ding, R.B.; Xuan, J.L.; et al. Robust Subsurface Biological Response During the Decaying Stage of an Extreme Indian Ocean Dipole in 2019. *Geophys. Res. Lett.* **2022**, *49*, e2022GL099721. [CrossRef]
24. Ma, X.Y.; Chen, G.X.; Li, Y.L.; Zeng, L.L. Interannual variability of sea surface chlorophyll a in the southern tropical Indian Ocean: Local versus remote forcing. *Deep Sea Res. Part I-Oceanogr. Res. Pap.* **2022**, *190*, 103914. [CrossRef]
25. Wiggert, J.D.; Hood, R.R.; Naqvi, S.W.A.; Brink, K.H.; Smith, S.L. Basin-wide modification of dynamical and biogeochemical processes by the positive phase of the Indian Ocean Dipole during the SeaWiFS era. *Indian Ocean. Biogeochem. Process. Ecol. Var.* **2009**, *185*, 385–407.

26. Chen, G.; Han, W.; Ma, X.; Li, Y.; Zhang, T.; Wang, D. Role of Extreme Indian Ocean Dipole in Regulating Three-Dimensional Freshwater Content in the Southeast Indian Ocean. *Geophys. Res. Lett.* **2023**, *50*, e2022GL102290. [CrossRef]
27. Du, Y.; Zhang, Y. Satellite and Argo observed surface salinity variations in the tropical Indian Ocean and their association with the Indian Ocean dipole mode. *J. Clim.* **2015**, *28*, 695–713. [CrossRef]
28. Liao, X.; Du, Y.; Wang, T.; He, Q.; Zhan, H.; Hu, S.; Wu, G. Extreme phytoplankton blooms in the southern tropical Indian Ocean in 2011. *J. Geophys. Res. Ocean.* **2020**, *125*, e2019JC015649. [CrossRef]
29. Kawamiya, M.; Oschlies, A.J.G.R.L. Formation of a basin-scale surface chlorophyll pattern by Rossby waves. *Geophys. Res. Lett.* **2001**, *28*, 4139–4142. [CrossRef]
30. Cai, W.; Santoso, A.; Wang, G.; Weller, E.; Wu, L.; Ashok, K.; Masumoto, Y.; Yamagata, T.J.N. Increased frequency of extreme Indian Ocean Dipole events due to greenhouse warming. *Nature* **2014**, *510*, 254–258. [CrossRef]
31. Cai, W.J.; Yang, K.; Wu, L.X.; Huang, G.; Santoso, A.; Ng, B.; Wang, G.J.; Yamagata, T. Opposite response of strong and moderate positive Indian Ocean Dipole to global warming. *Nat. Clim. Chang.* **2021**, *11*, 27–32. [CrossRef]
32. Saji, N.; Goswami, B.N.; Vinayachandran, P.; Yamagata, T.J.N. A dipole mode in the tropical Indian Ocean. *Nature* **1999**, *401*, 360–363. [CrossRef] [PubMed]
33. Fairall, C.W.; Bradley, E.F.; Hare, J.; Grachev, A.A.; Edson, J.B.J. Bulk parameterization of air–sea fluxes: Updates and verification for the COARE algorithm. *J. Clim.* **2003**, *16*, 571–591. [CrossRef]
34. Waga, H.; Hirawake, T.; Ueno, H. Impacts of Mesoscale Eddies on Phytoplankton Size Structure. *Geophys. Res. Lett.* **2019**, *46*, 13191–13198. [CrossRef]
35. Du, Y.; Chen, Z.; Xie, S.-P.; Zhang, L.; Zhang, Y.; Cai, Y. Drivers and characteristics of the Indo-western Pacific Ocean capacitor. *Front. Clim.* **2022**, *4*, 1014138. [CrossRef]
36. Sun, Q.; Zhang, Y.; Du, Y.; Jiang, X. Asymmetric response of sea surface salinity to extreme positive and negative indian ocean dipole in the southern tropical indian ocean. *J. Geophys. Res.-Ocean.* **2022**, *127*, e2022JC018986. [CrossRef]
37. Masumoto, Y.; Meyers, G. Forced Rossby waves in the southern tropical Indian Ocean. *J. Geophys. Res.-Ocean.* **1998**, *103*, 27589–27602. [CrossRef]
38. Zhang, Y.; Du, Y. Extreme IOD induced tropical Indian Ocean warming in 2020. *Geosci. Lett.* **2021**, *8*, 37. [CrossRef]